Visible-Light-Activated Type II Heterojunction in Cu$_3$(hexahydroxytriphenylene)$_2$/Fe$_2$O$_3$ Hybrids for Reversible NO$_2$ Sensing: Critical Role of $\pi-\pi^*$ Transition

Young-Moo Jo, Kyeorei Lim, Ji Won Yoon, Yong Kun Jo, Young Kook Moon, Ho Won Jang, and Jong-Heun Lee*

Read Online

ACCESS | 📊 Metrics & More | 📰 Article Recommendations | 🆂�isupporting Information

ABSTRACT: Metal−organic frameworks (MOFs) with high surface area, tunable porosity, and diverse structures are promising platforms for chemiresistors; however, they often exhibit low sensitivity, poor selectivity, and irreversibility in gas sensing, hindering their practical applications. Herein, we report that hybrids of Cu$_3$(HHTP)$_2$ (HHTP = 2,3,6,7,10,11-hexahydroxytriphenylene) nanoflakes and Fe$_2$O$_3$ nanoparticles exhibit highly sensitive, selective, and reversible detection of NO$_2$ at 20 °C. The key parameters to determine their response, selectivity, and recovery are discussed in terms of the size of the Cu$_3$(HHTP)$_2$ nanoflakes, the interaction between the MOFs and NO$_2$, and an increase in the concentration and lifetime of holes facilitated by visible-light photoactivation and charge-separating energy band alignment of the hybrids. These photoactivated MOF−oxide hybrids suggest a new strategy for designing high-performance MOF-based gas sensors.
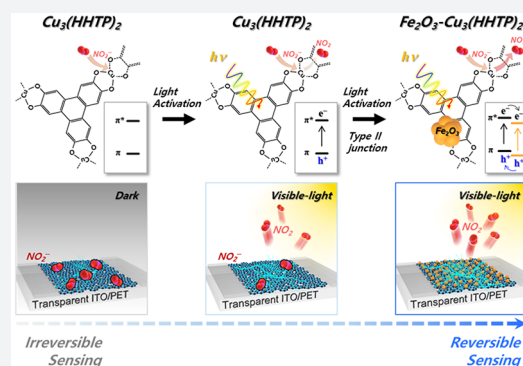
1. INTRODUCTION

Chemiresistors, including metal oxides, transition metal dichalcogenides, and carbon-based materials, provide a simple and cost-effective method for hazardous gas detection, environmental monitoring, and exhaled breath analysis.[1−4] Metal−organic frameworks (MOFs) with ultrahigh porosity, large surface area, and facile chemical tunability[5−8] have been considered as viable alternatives for the design of high-performance chemiresistors owing to the recent development of electrically conductive MOFs.[9] Furthermore, not only the metal ions/clusters but also the organic linkers of MOFs can interact with analyte gases, and controllable pore sizes can be used to tune the transport/sieving of gas molecules, enabling the tailored control of gas-sensing characteristics.[10−12]

In MOFs composed of two-dimensional (2D) ligands, delocalized charges can be generated from extended $\pi-d$ conjugation between the metal node and ligand, which improve conductivity.[9,13−16] Furthermore, the interaction between analyte gases and metal nodes or organic ligands can induce chemiresistive variation. Campbell et al. first reported the chemiresistive sensing of ammonia using Cu$_3$(HITP)$_2$ (HITP = 2,3,6,7,10,11-hexaiminotriphenylene),[17] and several studies have been conducted on the design of volatile organic compound sensors by replacing metal nodes (Cu) with Ni and Co or replacing triphenylene-based ligands with phthalocyanine-based ones.[18−24] Although the possibility of modulating the gas selectivity by compositional variation of MOFs has been explored, there remain many challenges such

as the requirement of high sensitivity and reversibility for the implementation of MOF-based gas sensors in practical applications. In particular, most MOFs exhibit dosimetric NO$_2$ sensing behavior;[22,25] thus, the reversible detection of NO$_2$ using chemiresistive MOFs has never been reported. Furthermore, the sensitive and selective detection of NO$_2$ using semiconducting MOFs has rarely been reported.

Herein, we report highly sensitive, selective, and reversible NO$_2$ sensors using Cu$_3$(HHTP)$_2$ (HHTP = 2,3,6,7,10,11-hexahydroxytriphenylene) conductive MOFs composed of copper metal ions and HHTP ligands in 2D hexagonal structures (Figure 1a). To enhance the gas accessibility, fine and well-dispersed Cu$_3$(HHTP)$_2$-nanoflakes (NFs) were separated from coarse and agglomerated Cu$_3$(HHTP)$_2$-bulk (B) flakes by centrifugation. At room temperature, Cu$_3$(HHTP)$_2$-NFs exhibited a significantly higher response to NO$_2$ than Cu$_3$(HHTP)$_2$-B flakes (Figure 1b). The visible-light photoactivation of MOFs substantially improved the recovery after NO$_2$ sensing by promoting gas desorption at room temperature (Figure 1c). Furthermore, hybrids between
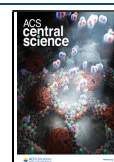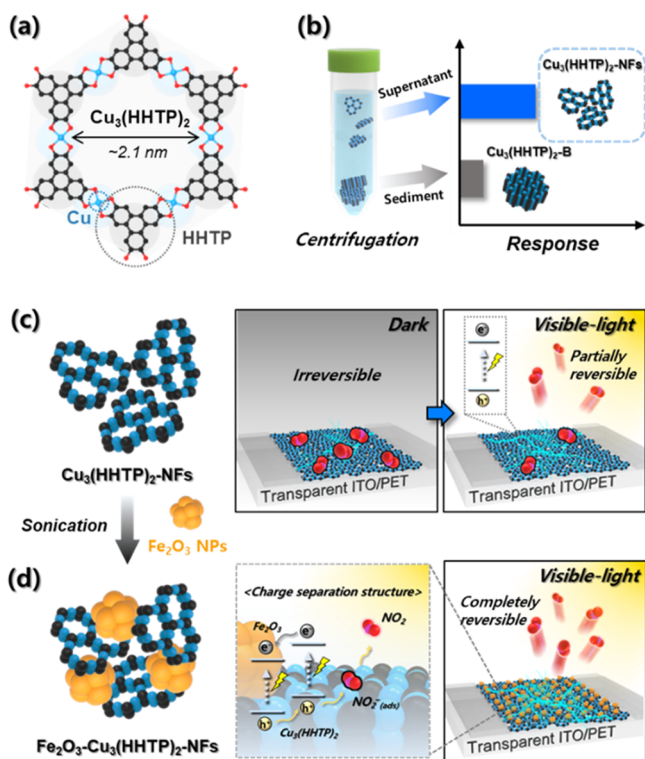
Figure 1. (a) Crystal structure of $Cu_3(HHTP)_2$. (b) Separation of highly sensitive $Cu_3(HHTP)_2$-NFs sensors by centrifugation. (c) Photoactivation of the recovery reaction after NO_2 sensing. (d) Reversible and selective NO_2 sensors using $Fe_2O_3-Cu_3(HHTP)_2$-NFs hybrids with charge-separating energy band alignment.

$Cu_3(HHTP)_2$-NFs and Fe_2O_3 nanoparticles (NPs) with a charge-separating type (II) energy band alignment have been

suggested to achieve complete and rapid recovery assisted by effective charge separation (Figure 1d). To the best of our knowledge, this is the first report on the design of a highly sensitive, selective, and reversible MOF-based NO_2 sensor through photoactivation of the sensing/recovery reaction and the establishment of energy band alignments to prolong the lifetime of charge carriers.

2. RESULTS AND DISCUSSION

Polycrystalline $Cu_3(HHTP)_2$ flakes (referred to as $Cu_3(HHTP)_2$-Fs) were prepared by a solvothermal reaction (Figure 2a, Figure S1 in the Supporting Information). High-resolution transmission electron microscopy (TEM) image revealed a hexagonal microporous structure of $Cu_3(HHTP)_2$ (pore size: ~2.1 nm) (Figure 2b). To systematically investigate the particle size dependence of the gas-sensing characteristics, $Cu_3(HHTP)_2$-Fs were sorted using differential velocity centrifugation (Figure S2). Centrifugation was performed at a speed of 10 000 rpm to obtain supernatants composed of small flakes (referred to as $Cu_3(HHTP)_2$-10000), and the sediments were redispersed for subsequent separation. In the same way, flakes were separated at 5000, 3000, 1000, 500, 300, 100, and 50 rpm to collect supernatants (referred to as $Cu_3(HHTP)_2$-ω, ω = 5000−50) and the remaining sediment composed of coarse flakes (referred to as $Cu_3(HHTP)_2$-0). The UV/vis spectra of the $Cu_3(HHTP)_2$-ω specimens (Figure S3) reveal a distribution of yields (Figure S4a). However, no peak shift was found in any of the specimens (Figure S3), confirming that each specimen comprised the same material at different sizes. The amount of $Cu_3(HHTP)_2$-10000 was too small to conduct a size analysis and fabricate a gas sensor. Thus, the sizes and gas-sensing characteristics of $Cu_3(HHTP)_2$-ω (ω = 5000−0) were measured and compared. The average size of $Cu_3(HHTP)_2$-5000 determined by
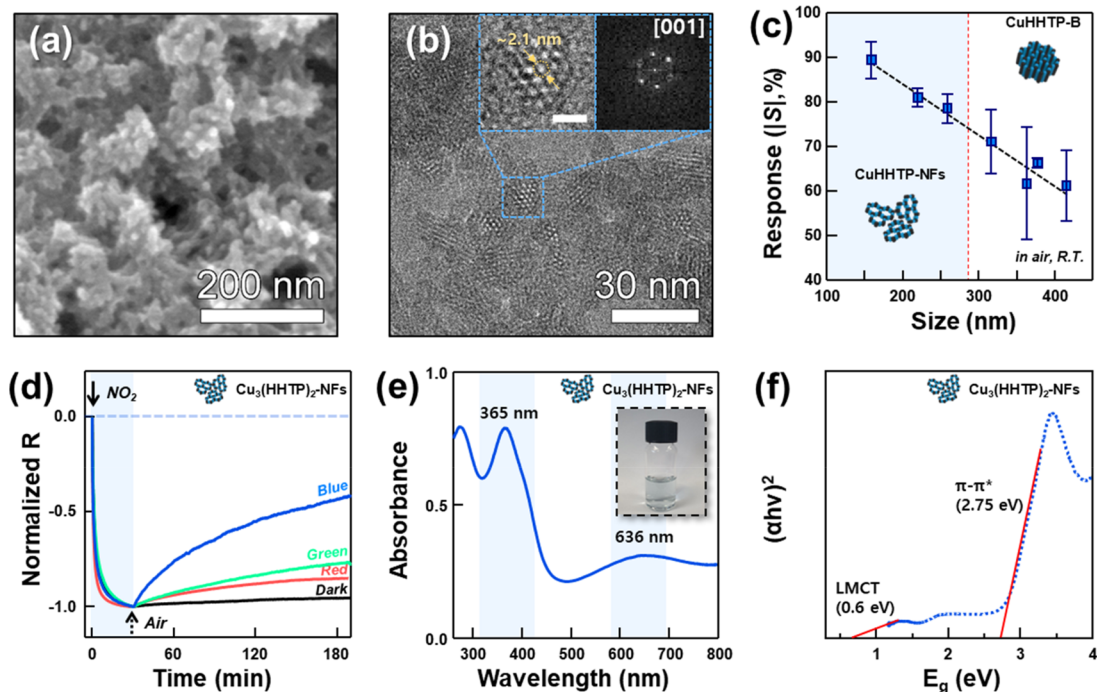
Figure 2. (a) SEM images and (b) TEM images of $Cu_3(HHTP)_2$-Fs. (c) Size-dependent NO_2 sensing characteristics of the $Cu_3(HHTP)_2$-ω (ω = 10000−0) sensor. The error bars were calculated from the responses of 3 different sensors. (d) Normalized sensing transients of $Cu_3(HHTP)_2$-NFs sensor to NO_2 under different illumination conditions (dark, red, green, and blue). (e) UV/vis spectra and (f) Tauc plot of $Cu_3(HHTP)_2$-NFs.
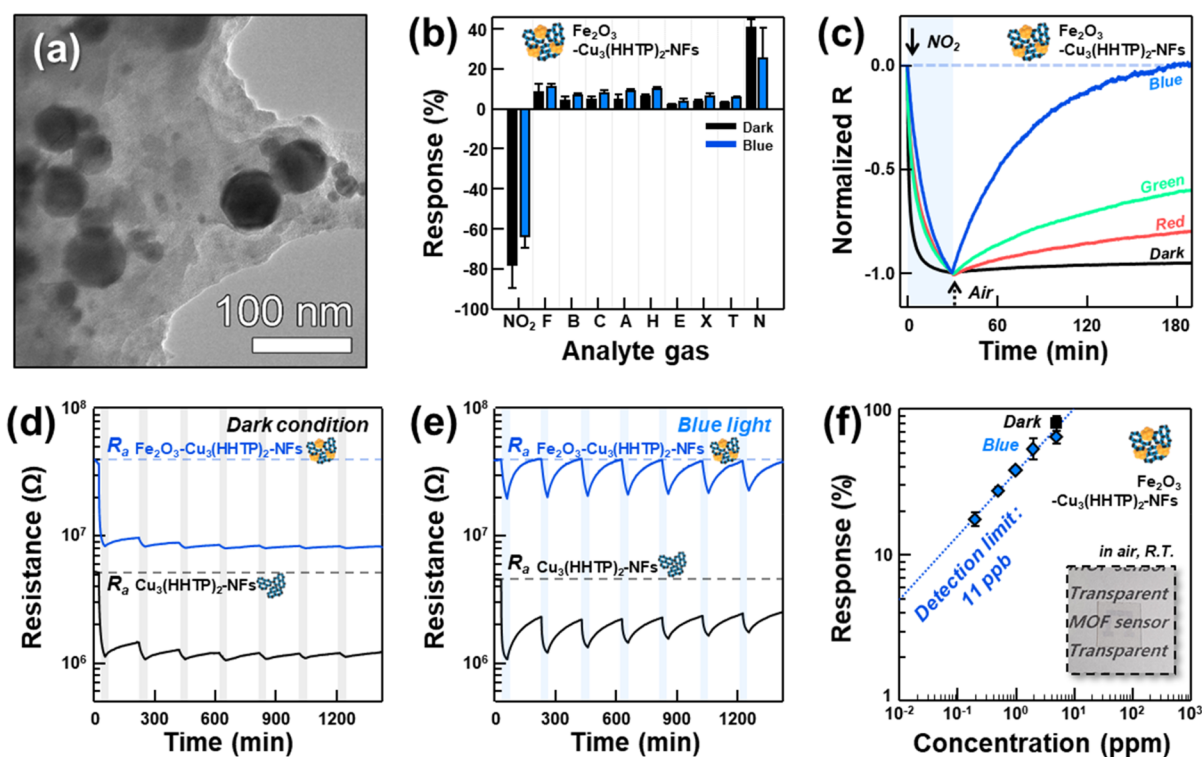
Figure 3. (a) TEM images of Fe$_2$O$_3$–Cu$_3$(HHTP)$_2$-NFs. (b) Gas responses of the Fe$_2$O$_3$–Cu$_3$(HHTP)$_2$-NFs sensor to 5 ppm of NO$_2$, HCHO (F), benzene (B), CO (C), acetone (A), H$_2$ (H), ethanol (E), p-xylene (X), toluene (T), and ammonia (N) under dark conditions and blue light illumination. (c) Normalized sensing transients of the Fe$_2$O$_3$–Cu$_3$(HHTP)$_2$-NF sensor to 5 ppm of NO$_2$ under different illumination conditions (dark, red, green, and blue). (d, e) 7 repetitive sensing transients of the Cu$_3$(HHTP)$_2$-NFs and Fe$_2$O$_3$–Cu$_3$(HHTP)$_2$-NFs sensors to 5 ppm of NO$_2$ under dark conditions and blue light illumination. (f) Response of Fe$_2$O$_3$–Cu$_3$(HHTP)$_2$-NFs sensors to 0.2–5 ppm of NO$_2$ under blue light illumination (blue diamond) and to 5 ppm of NO$_2$ under dark conditions. The error bars in parts b and f were calculated from the gas responses of three different sensors.

dynamic light scattering was 158.7 ± 2.4 nm, and the particle size increased to 415.3 ± 16.9 nm as the separation speed decreased (Figure S4b). The responses $[S = \Delta R/R_a \times 100\% = (R_g - R_a)/R_a \times 100\%$; R_g, resistance in gas; R_a, resistance in air] of Cu$_3$(HHTP)$_2$-ω sensors to 5 ppm of NO$_2$ were measured at room temperature under dark conditions (Figure 2c and Figure S5). The Cu$_3$(HHTP)$_2$-5000 sensor demonstrated the highest response of 89.4% among the investigated sensors, and the response gradually decreased to 61.1% as the particle size increased. This is consistent with a previous report stating that the ammonia response of thin 2D triphenylene-based MOFs (~10 layers) is superior to that of MOFs with a thicker and agglomerated configuration.[26] In conductive MOFs, analyte gases are known to interact with the metal node or functional groups of ligands and change the resistance by the exchange of charges.[18−21] From this perspective, the higher response of the smaller Cu$_3$(HHTP)$_2$ can be attributed to more interaction between the gas and the reaction sites of MOFs with high surface areas.

To simplify the classification procedure, Cu$_3$(HHTP)$_2$-Fs were divided into two parts based on a fixed centrifugation speed of 1000 rpm. The Cu$_3$(HHTP)$_2$-NFs are the supernatants, and Cu$_3$(HHTP)$_2$-B are the sediments (Figure S6). The surface area of Cu$_3$(HHTP)$_2$-NFs (48.5 m^2 g^{-1}) was 2.4 times higher than that of Cu$_3$(HHTP)$_2$-B (20.3 m^2 g^{-1}) (Figure S7). The gas responses of the Cu$_3$(HHTP)$_2$-NFs sensor to 5 ppm of analyte gases, such as nitrogen dioxide (NO$_2$), formaldehyde (HCHO), benzene (C$_6$H$_6$), carbon monoxide (CO), acetone (C$_3$H$_6$O), hydrogen (H$_2$), ethanol

(C$_2$H$_5$OH), p-xylene (C$_8$H$_{10}$), toluene (C$_7$H$_8$), and ammonia (NH$_3$), were measured at room temperature under dark conditions. The sensor exhibited chemiresistive variation of p-type semiconductors: a decrease and increase in resistance upon exposure to oxidizing (NO$_2$) and reducing gases (other gases), respectively (Figure S8b). The response to NO$_2$ ($S = -79.8\%$) was not only opposite to but also significantly higher than those of the other nine gases (Figure S8a), demonstrating selective NO$_2$ detection. The high selectivity can be attributed to Lewis acid−base reactions between the metal node and the NO$_2$. In general, the transition metal Cu^{II} accepts electrons from neutral or basic gases to fill the unoccupied d orbital.[27,28] In contrast, highly acidic NO$_2$ extracts electrons from Cu^I by forming a coordination complex with Cu^I [(1) N-nitro, (2) O-nitrito, or (3) O,O′ bidentate] if Cu^I is present.[29,30] Thus, the NO$_2$ adsorption reaction increases the hole concentration.

$$NO_{2(g)} \leftrightarrow NO^-_{2(ads)} + h^+ \tag{1}$$

It is worth noting that the sensing transient of NO$_2$ shows irreversible behavior, whereas those of other reducing gases, except NH$_3$, return to the baseline (Figure S8b). Irreversible NO$_2$ sensing behavior is commonly observed in all of the sensors in Figure S5, regardless of particle size, suggesting that it is an inherent sensing characteristic. This is consistent with the NO$_2$ sensing results of most MOF-based chemiresistors in the literature.[22,25] This irreversibility after NO$_2$ sensing can be explained by the formation of a stable coordination complex between Cu and NO$_2$,[29,30] which impedes the use of Cu$_3$(HHTP)$_2$ as a NO$_2$ sensor. Because NO$_2$ sensing involves

the formation of $NO_{2(ads)}^-$, more holes need to be provided to promote recovery. Considering the semiconducting nature and energy band gap of $Cu_3(HHTP)_2$, the photogeneration of charge carriers can be adopted to facilitate recovery. For this, NO_2-sensing transients of $Cu_3(HHTP)_2$-NFs were measured under illumination by LED lamps of different colors: red (E_{red} = 1.97 eV; irradiance, 0.25 W m^{-2}), green (E_{green} = 2.34 eV; irradiance, 0.15 W m^{-2}), and blue (E_{blue} = 2.76 eV; irradiance, 0.15 W m^{-2}). The recovery rate of the $Cu_3(HHTP)_2$-NFs sensor in normalized sensing transients (Figure 2d) substantially increased in the order dark condition < red < green < blue light, in proportion to the photon energy, confirming the validity of photoactivation. This is supported by the fact that the sensor resistance tends to decrease with an increase in the photon energy of the light (Figure S9).

UV/vis spectra of the $Cu_3(HHTP)_2$-NFs exhibit distinct absorption peaks at 365 and 636 nm (Figure 2e). The two energy states of $Cu_3(HHTP)_2$ were determined by fitting the Tauc plot (Figure 2f). First, the state at near-infrared energy (0.60 eV) is associated with the ligand-to-metal charge transfer (LMCT) transition, which enables conduction in $Cu_3(HHTP)_2$ at room temperature. The second energy state in the visible region (2.75 eV) is related to the $\pi-\pi^*$ transition of the HHTP link,[31,32] explaining the promotion of the recovery reaction under blue light illumination (Figure 2f).

For quantitative analysis of reaction kinetics, the reaction constants for the adsorption and desorption of $NO_{2(ads)}^-$ (k_{ads} and k_{des}) was calculated by exponential fitting of dynamic sensing transients ($S(t)$) using the following eqs 2 and 3, where S_{max} is the maximum response, and C_{NO_2} is the concentration of NO_2. This calculation is based on the continuum site balance equations in that the response (S) is proportional to the NO_2 and is explored using the mass action law of chemisorbed NO_2 on $Cu_3(HHTP)_2$.[33]

NO_2 adsorption reaction

$$S(t) = S_{max} \frac{C_{NO_2}(k_{ads}/k_{des})}{1 + C_{NO_2}(k_{ads}/k_{des})} \left[1 - \exp\left(\frac{1 + C_{NO_2}(k_{ads}/k_{des})}{(k_{ads}/k_{des})} k_{ads} t \right) \right] \qquad (2)$$

NO_2 desorption reaction

$$S(t) = S_{max} \exp(-k_{des}t) \qquad (3)$$

The k_{des} value of the $Cu_3(HHTP)_2$-NFs sensor under blue light (1.41×10^{-4} s^{-1}) was approximately 2.5 times higher than that under dark conditions (5.74×10^{-5} s^{-1}) (Figure S10), further indicating that the recovery is significantly promoted by illumination with blue light. Although the NO_2 response under blue light illumination is slightly lower than that under dark conditions (S = −68.9%), it is still significantly higher than those of the other nine gases (Figure S11). It should be pointed out that the $Cu_3(HHTP)_2$-NFs sensor did not exhibit complete recovery after NO_2 sensing even under blue light with the highest energy. This suggests that the recombination of photogenerated electron−hole pairs occurs before promoting the desorption of $NO_{2(ads)}^-$, possibly due to the relatively low mobility of electrons and holes and the presence of defects in $Cu_3(HHTP)_2$.

The establishment of heterostructures with charge-separating energy band structures, which are frequently employed in the design of photocatalysts, can be used to prolong the lifetimes of electrons and holes by charge separation.[34] To examine this effect, a sensor using $Fe_2O_3-Cu_3(HHTP)_2$

heterostructures was fabricated (Figure 3a, Figure S12). Fe_2O_3 was chosen because it exhibits an appropriate band structure to facilitate the charge separation at the hetero-interfaces. The $Cu_3(HHTP)_2$-NFs were dispersed in deionized water, which was uniformly mixed with Fe_2O_3 NPs (<50 nm) ($Cu_3(HHTP)_2$-NFs:Fe_2O_3 NPs = 2:1 by weight) by sonication (referred to as $Fe_2O_3-Cu_3(HHTP)_2$-NFs). The response of the $Fe_2O_3-Cu_3(HHTP)_2$-NFs sensor to NO_2, as well as to the nine other gases, was similar to that of the $Cu_3(HHTP)_2$-NFs sensor (Figure 3b, Figure S13). The NO_2 selectivity under red and green lights remained similar (Figures S14 and S15). This indicates that the chemiresistive variation of the $Fe_2O_3-Cu_3(HHTP)_2$-NFs sensor is primarily due to the continuous structure of $Cu_3(HHTP)_2$-NFs, while the discretely decorated Fe_2O_3 NPs on the $Cu_3(HHTP)_2$-NFs do not play a role in establishing an additional conduction path or contribute to the chemiresistive variation or enhancing the catalytic promotion of the sensing reaction. Interestingly, decoration by Fe_2O_3 NPs significantly improved the recovery of the $Cu_3(HHTP)_2$-NFs sensor under the illumination of red, green, and blue LED light (Figure 3c). In particular, the $Fe_2O_3-Cu_3(HHTP)_2$-NFs sensor showed completely reversible NO_2 sensing characteristics (Figure 3c) and a significantly high k_{des} value under blue light (Figure S16). The optimized NO_2 recovery was obtained when the weight ratio of $Cu_3(HHTP)_2$-NFs and Fe_2O_3 was 2:1 (Figure S17). The promotion of the recovery reaction by blue light is also supported by the observation that the lower light intensity led to the more sluggish recovery (Figure S18). To confirm the effect of photoactivation on the reversible sensing behaviors, the seven repetitive NO_2 sensing transients of $Cu_3(HHTP)_2$-NFs and $Fe_2O_3-Cu_3(HHTP)_2$-NFs sensors were measured under dark conditions and blue light illumination (Figure 3d,e). Under dark conditions, the $Cu_3(HHTP)_2$-NFs and $Fe_2O_3-Cu_3(HHTP)_2$-NFs sensors barely recovered after the first NO_2 sensing. In contrast, under blue light illumination, the $Cu_3(HHTP)_2$-NFs sensor showed improved recovery, and the $Fe_2O_3-Cu_3(HHTP)_2$-NFs sensor exhibited a completely reversible behavior. This clearly verifies that the heterojunction between Fe_2O_3 NPs and $Cu_3(HHTP)_2$-NFs promotes the desorption of $NO_{2(ads)}^-$ by increasing the number of photoinduced holes and their lifetime. The response of the $Fe_2O_3-Cu_3(HHTP)_2$-NFs sensor to 0.2−5 ppm of NO_2 was measured at room temperature under blue light (Figure 3f and Figure S19). The low detection limit of $Fe_2O_3-Cu_3(HHTP)_2$-NFs sensors to NO_2 was calculated to be 11 ppb when a signal-to-noise ratio >10 was used as the criterion for gas sensing. The NO_2 response in the present study was superior to those of most other sensors using mesoporous oxides, carbon-based materials, and MOFs in the literature (Table S1). It is worth noting that the particle size distribution of $Cu_3(HHTP)_2$-NFs is relatively wide, which might be a reason for the fluctuation of the gas response. In this perspective, the accuracy of the gas response can be enhanced by using $Cu_3(HHTP)_2$ with a monodisperse flake size. In addition, the sensor exhibited the mild variation of the NO_2 response with changing the humidity from dry to relative humidity 50% atmosphere or varying the sensor temperature from 14 to 34 °C, demonstrating the potential of sensor operation under different ambient conditions (Figure S20).

Furthermore, the static NO_2 gas-sensing characteristics under natural sunlight were investigated using an acrylic chamber at 50% RH and 3 °C (Figure S21 and Video S1). Completely reversible sensing with a high response value of
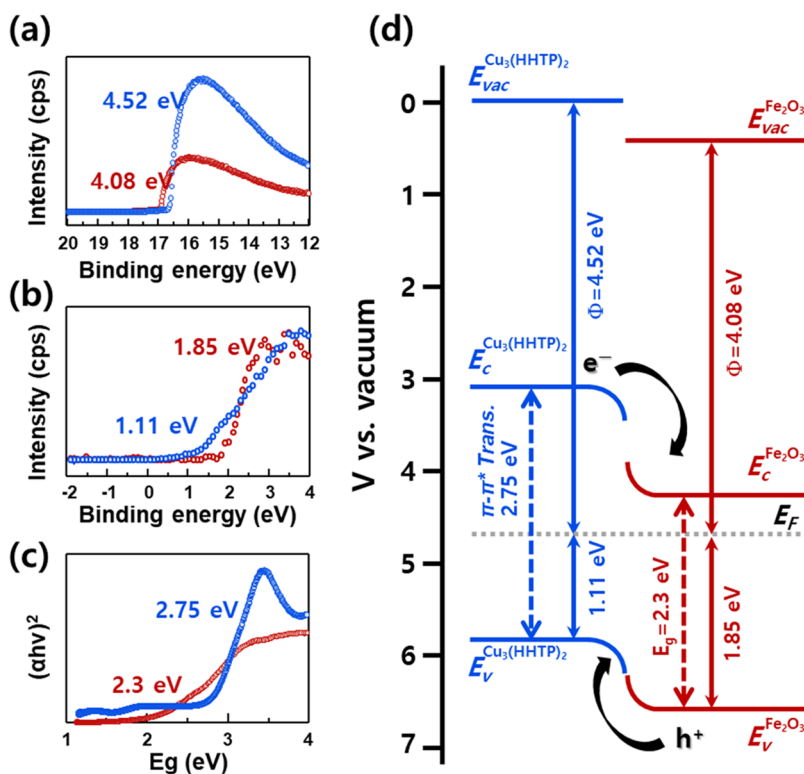
Figure 4. (a) UPS spectra, (b) XPS spectra, and (c) UV−vis spectra of $Cu_3(HHTP)_2$ and Fe_2O_3. (d) Schematic energy band diagram of the $Cu_3(HHTP)_2/Fe_2O_3$ heterojunction.

30.4% upon exposure to 40 ppb of NO_2 was achieved. NO_2 is a representative air pollutant generated from combustion reactions and diesel engines which can cause respiratory diseases in humans and induce photochemical smog, such as ozone.[35,36] The simple structure of the present sensor can be used for environmental monitoring at room temperature. Finally, the transparent (inset Figure 3f) and flexible design increases the prospects of achieving wearable gas sensors. It is worth noting that the transparency and flexibility of sensors can be enhanced further by the epitaxial growth of ultrathin 2D MOF films.[24]

To understand the origin of the charge-separating electronic structures, the Fe_2O_3 NPs and $Cu_3(HHTP)_2$-NFs were analyzed by ultraviolet photoelectron spectroscopy (UPS), X-ray photoelectron spectroscopy (XPS), and UV/vis spectroscopy. The work functions of $Cu_3(HHTP)_2$-NFs and Fe_2O_3 NPs were calculated to be 4.50 and 4.08 eV, respectively, from the secondary electron cutoff in the UPS spectra (Figure 4a). From the XPS spectra of $Cu_3(HHTP)_2$-NFs and Fe_2O_3 NPs, the energy differences between the valence-band maximum and Fermi energy were determined to be 1.11 and 1.85 eV, respectively (Figure 4b). Considering the two energy states (0.60 and 2.75 eV) associated with the LMCT and $\pi-\pi^*$ transition, both type I and type II band alignments can be established across the $Cu_3(HHTP)_2$ and Fe_2O_3 heterojunction (Figure 4d and Figure S22). Under blue light illumination, both band alignments are advantageous for photoinduced holes to transfer from the E_v of Fe_2O_3 NPs to the E_v of $Cu_3(HHTP)_2$-NFs because the valence band of $Cu_3(HHTP)_2$-NFs (5.63 eV vs vacuum) is more positive than that of Fe_2O_3 NPs (6.37 eV vs vacuum) (Figure 4d and Figure S22). This favors the desorption of $NO_{2(ads)}^-$. In particular, in type II band alignments, the recombination of photogenerated charges can be suppressed by transferring the electrons from the E_c of $Cu_3(HHTP)_2$-NFs to the E_c of Fe_2O_3, which prolongs the lifetime of the holes in the $Cu_3(HHTP)_2$-NFs and further facilitates the desorption of $NO_{2(ads)}^-$ (Figure 4d).

3. CONCLUSIONS

In summary, the size sorting of $Cu_3(HHTP)_2$ flakes by differential velocity centrifugation confirmed that fine nanoflakes with abundant reaction sites on the surface exhibited a higher NO_2 response (89.4%) than coarse flakes (61.1%). Nanoflakes of $Cu_3(HHTP)_2$ barely reacted with nine other interference gases but exhibited irreversible NO_2 sensing due to the formation of a stable coordination complex. Visible-light photoactivation has been suggested as an effective way to improve recovery. The NO_2 recovery rate increased in proportion to the photon energy of the LED lamp color (red, 1.97 eV; green, 2.34; and blue, 2.76 eV). Furthermore, hybrids between $Cu_3(HHTP)_2$ and Fe_2O_3 with charge-separating electronic structures significantly increased the concentration and lifetime of holes in $Cu_3(HHTP)_2$, which enabled highly sensitive, selective, and reversible detection of NO_2. The strategy based on the photoactivation of MOF−oxide hybrids paves the way for the design of high-performance MOF-based gas sensors with new functionalities.

4. EXPERIMENTAL METHODS

4.1. Materials. 2,3,6,7,10,11-Hexahydroxytriphenylene (H_6HHTP, $C_{18}H_{12}O_6 \cdot xH_2O$, 95.0%) was purchased from Tokyo Chemical Industry. Copper(II) nitrate hydrate ((Cu-$(NO_3)_2 \cdot xH_2O$, 99.999%) and iron(III) oxide nanopowders (Fe_2O_3, <50 nm) were purchased from Sigma-Aldrich. All reagents were used without further purification.

4.2. Preparation of Cu$_3$(HHTP)$_2$-Fs. A methanol solution (3 mL) containing 25 mg of H$_6$HHTP was mixed with 57 mL of an aqueous solution containing 60 mg of copper(II) nitrate hydrate by vigorous stirring for 5 min. This solution was transferred to a 100 mL Teflon-lined stainless-steel autoclave, and a solvothermal reaction was allowed to proceed at 70 °C for 12 h. The produced dark blue precipitate was washed twice with ethanol and three times with deionized (DI) water via centrifugation at 15 000 rpm and subsequently redispersed in DI water (3 mg mL^{-1}).

4.3. Preparation of Cu$_3$(HHTP)$_2$-ω. The Cu$_3$(HHTP)$_2$-Fs were sorted by size using a differential velocity centrifugation method. First, 5 mL of slurry containing Cu$_3$(HHTP)$_2$ flakes (3 mg mL^{-1}) was diluted with 20 mL of DI water and centrifuged at 10 000 rpm for 1 h. The supernatants were carefully collected, and the sediments were redispersed in 25 mL of DI water for subsequent centrifugation. Similarly, different sizes of Cu$_3$(HHTP)$_2$ particles were collected at centrifugation speeds of 5000, 3000, 1000, 500, 300, 100, and 50 rpm by collecting supernatants, and the final sediments were redispersed in 25 mL of DI water.

4.4. Preparation of Cu$_3$(HHTP)$_2$-NFs. The Cu$_3$(HHTP)$_2$-Fs were separated into two groups: Cu$_3$(HHTP)$_2$ nanoflakes and Cu$_3$(HHTP)$_2$-bulk flakes. For this, 5 mL of slurry containing Cu$_3$(HHTP)$_2$ flakes (3 mg mL^{-1}) was diluted with 20 mL of DI water and centrifuged at 1000 rpm for 3 h. The supernatants (Cu$_3$(HHTP)$_2$-NFs) were carefully collected, and the sediments (Cu$_3$(HHTP)$_2$-B) were redispersed in 25 mL of DI water.

4.5. Preparation of Fe$_2$O$_3$−Cu$_3$(HHTP)$_2$-NFs. Fe$_2$O$_3$ nanoparticles (NPs) (1 mg) were dispersed in 10 mL of DI water by sonication for 30 min. The slurry of well-dispersed Fe$_2$O$_3$ NPs (1 mL, 0.1 mg mL^{-1}) was mixed with 1 mL of Cu$_3$(HHTP)$_2$-NFs slurry (0.2 mg mL^{-1}) to obtain a 2:1 weight ratio of Cu$_3$(HHTP)$_2$-NFs to Fe$_2$O$_3$ NP hybrid structures by sonication for 30 min.

4.6. Characterization Methods. The structure and morphology of the materials were investigated using field-emission scanning electron microscopy (FE-SEM, Su-70, Hitachi Co. Ltd.) and high-resolution transmission electron microscopy (HR-TEM, Titan, FEI Co. Ltd.). The phase and crystallinity of the materials were analyzed using X-ray diffraction (XRD, D/Max-2500 V/Pc, Rigaku). Absorbance spectra of the materials were measured using a UV−vis spectrophotometer (Cary 50, Agilent Technologies Inc.). The sizes of the materials were investigated by dynamic light scattering using a ζ potential and particle size analyzer (ELSZ-2000ZS, Otsuka Electronics Co. Ltd.). The specific surface areas were measured by Brunauer−Emmett−Teller analysis of N$_2$ adsorption isotherms (BET, Tristar 3000, Micromeritics, Co. Ltd.). The electronic band structures were characterized by ultraviolet photoemission spectroscopy (UPS, AXIS-Nova, Kratos Analytical Ltd.; monochromatic He I = 21.2 eV, Ag 3d$_{5/2}$ < 100 meV) and X-ray photoelectron spectroscopy (XPS, AXIS-Nova, Kratos Analytical Ltd.; monochromatic Al Kα = 1486.6 eV, Ag 3d$_{5/2}$ < 0.48 eV), and a Tauc plot was established from the UV−vis spectra.

4.7. Gas-Sensing Characteristics. The slurry containing Cu$_3$(HHTP)$_2$-NFs (0.1 mg mL^{-1}) was deposited onto transparent PET substrates (size: 8 mm × 8 mm) with a patterned indium tin oxide interdigitated electrode (gap: 5 μm) by drop casting. The sensors were heat-treated at 60 °C for 0.5 h to remove the solvent. The gas-sensing characteristics were measured at room temperature, and the sensors were placed in a square quartz tube (size: 3 × 3 × 3 cm^3). The atmosphere was controlled using a four-way valve to ensure a constant flow rate (200 cm^3 min^{-1}) of synthetic air and analyte gases [5 ppm of nitrogen dioxide (NO$_2$), formaldehyde (HCHO), benzene (C$_6$H$_6$), carbon monoxide (CO), acetone (C$_3$H$_6$O), hydrogen (H$_2$), ethanol (C$_2$H$_5$OH), p-xylene (C$_8$H$_{10}$), toluene (C$_7$H$_8$), and ammonia (NH$_3$)]. MR16 commercial LED lamps (red, green, and blue) were installed at a distance of 2 cm from the sensors, and the sensor was stabilized in air for 6 h. The two-probe direct-current resistance of the sensor was obtained using an electrometer.

■ ASSOCIATED CONTENT

ⓢ Supporting Information

The Supporting Information is available free of charge at https://pubs.acs.org/doi/10.1021/acscentsci.1c00289.

> XRD analysis, schematic experimental procedures for preparing sensing materials, UV/vis analysis, yields and size distribution of sensing materials, gas-sensing characteristics, pore size distribution, specific surface area, sensor resistances under different colors of LED lights, calculation of adsorption and desorption rate constants, SEM images, schematic images of the outdoor chamber system, and an energy band diagram (PDF)

> Video S1: Static NO$_2$ gas-sensing characteristics under natural sunlight investigated using an acrylic chamber at 50% RH and 3 °C (MP4)

■ AUTHOR INFORMATION

Corresponding Author

Jong-Heun Lee − *Department of Materials Science and Engineering, Korea University, Seoul 02841, Republic of Korea;* ⓞ orcid.org/0000-0002-3075-3623; Phone: +82-2-3290-3282; Email: jongheun@korea.ac.kr; Fax: +82-2-928-3584

Authors

Young-Moo Jo − *Department of Materials Science and Engineering, Korea University, Seoul 02841, Republic of Korea*

Kyeorei Lim − *Department of Materials Science and Engineering, Korea University, Seoul 02841, Republic of Korea*

Ji Won Yoon − *Department of Materials Science and Engineering, Korea University, Seoul 02841, Republic of Korea*

Yong Kun Jo − *Department of Materials Science and Engineering, Korea University, Seoul 02841, Republic of Korea*

Young Kook Moon − *Department of Materials Science and Engineering, Korea University, Seoul 02841, Republic of Korea*

Ho Won Jang − *Department of Materials Science and Engineering, Research Institute of Advanced Materials Seoul National University, Seoul 08826, Republic of Korea;* ⓞ orcid.org/0000-0002-6952-7359

Complete contact information is available at:
https://pubs.acs.org/10.1021/acscentsci.1c00289

Notes

The authors declare no competing financial interest.

ACKNOWLEDGMENTS

REFERENCES

(1) Jeong, S.-Y.; Kim, J.-S.; Lee, J.-H. Rational Design of Semiconductor-Based Chemiresistors and their Libraries for Next-Generation Artificial Olfaction. *Adv. Mater.* **2020**, *32*, 2002075.

(2) Moon, Y. K.; Jeong, S.-Y.; Jo, Y.-M.; Kang, Y. C.; Lee, J.-H. Highly Selective Detection of Benzene and Discrimination of Volatile Aromatic Compounds Using Oxide Chemiresistors with Tunable Rh-TiO$_2$ Catalytic Overlayers. *Adv. Sci.* **2021**, *8*, 2004078.

(3) Kim, Y.; Kim, T.; Lee, J.; Choi, Y. S.; Moon, J.; Park, S. Y.; Lee, T. H.; Park, H. K.; Lee, S. A.; Kwon, M. S.; Byun, H.-G.; Lee, J.-H.; Lee, M.-G.; Hong, B. H.; Jang, H. W. Tailored Graphene Micropatterns by Wafer-Scale Direct Transfer for Flexible Chemical Sensor Platform. *Adv. Mater.* **2021**, *33*, 2004827.

(4) Wu, J.; Tao, K.; Guo, Y.; Li, Z.; Wang, X.; Luo, Z.; Feng, S.; Du, C.; Chen, D.; Miao, J.; Norford, L. K. A 3D Chemically Modified Graphene Hydrogel for Fast, Highly Sensitive, and Selective Gas Sensor. *Adv. Sci.* **2017**, *4*, 1600319.

(5) Rosi, N. L.; Eckert, J.; Eddaoudi, M.; Vodak, D. T.; Kim, J.; O'Keeffe, M.; Yaghi, O. M. Hydrogen Storage in Microporous Metal-Organic Frameworks. *Science* **2003**, *300*, 1127−1129.

(6) Furukawa, H.; Ko, N.; Go, Y. B.; Aratani, N.; Choi, S. B.; Choi, E.; Yazaydin, A. Ö.; Snurr, R. Q.; O'Keeffe, M.; Kim, J.; Yaghi, O. M. Ultrahigh Porosity in Metal-Organic Frameworks. *Science* **2010**, *329*, 424−428.

(7) Furukawa, H.; Cordova, K. E.; O'Keeffe, M.; Yaghi, O. M. The Chemistry and Applications of Metal-Organic Frameworks. *Science* **2013**, *341*, 1230444.

(8) Zhou, H.-C.; Long, J. R.; Yaghi, O. M. Introduction to Metal-Organic Frameworks. *Chem. Rev.* **2012**, *112*, 673−674.

(9) Xie, L. S.; Skorupskii, G.; Dincă, M. Electrically Conductive Metal-Organic Frameworks. *Chem. Rev.* **2020**, *120*, 8536−8580.

(10) Stassen, I.; Burtch, N.; Talin, A.; Falcaro, P.; Allendorf, M.; Ameloot, R. An Updated Roadmap for The Integration of Metal-Organic Frameworks with Electronic Devices and Chemical Sensors. *Chem. Soc. Rev.* **2017**, *46*, 3185.

(11) Hu, Z.; Deibert, B. J.; Li, J. Luminescent Metal-Organic Frameworks for Chemical Sensing and Explosive Detection. *Chem. Soc. Rev.* **2014**, *43*, 5815−5840.

(12) Koo, W.-T.; Jang, J.-S.; Kim, I.-D. Metal-Organic Frameworks for Chemiresistive Sensors. *Chem.* **2019**, *5*, 1938−1963.

(13) Sheberla, D.; Sun, L.; Blood-Forsythe, M. A.; Er, S.; Wade, C. R.; Brozek, C. K.; Aspuru-Guzik, A.; Dincă, M. High Electrical Conductivity in Ni$_3$(2,3,6,7,10,11-hexaiminotriphenylene)$_2$, a Semi-conducting Metal-Organic Graphene Analogue. *J. Am. Chem. Soc.* **2014**, *136*, 8859−8862.

(14) Hmadeh, M.; Lu, Z.; Liu, Z.; Gándara, F.; Furukawa, H.; Wan, S.; Augustyn, V.; Chang, R.; Liao, L.; Zhou, F.; Perre, E.; Ozolins, V.; Suenaga, K.; Duan, X.; Dunn, B.; Yamamto, Y.; Terasaki, O.; Yaghi, O. M. New Porous Crystals of Extended Metal-Catecholates. *Chem. Mater.* **2012**, *24*, 3511−3513.

(15) Dong, R.; Han, P.; Arora, H.; Ballabio, M.; Karakus, M.; Zhang, Z.; Shekhar, C.; Adler, P.; Petkov, P. S.; Erbe, A.; Mannsfeld, S. C. B.; Felser, C.; Heine, T.; Bonn, M.; Feng, X.; Cánovas, E. High-Mobility Band-Like Charge Transport in a Semiconducting Two-Dimensional Metal-Organic Framework. *Nat. Mater.* **2018**, *17*, 1027−1032.

(16) Huang, X.; Sheng, P.; Tu, Z.; Zhang, F.; Wang, J.; Geng, H.; Zou, Y.; Di, C.-A.; Yi, Y.; Sun, Y.; Xu, W.; Zhu, D. A Two-Dimensional π-d Conjugated Coordination Polymer with Extremely High Electrical Conductivity and Ambipolar Transport Behaviour. *Nat. Commun.* **2015**, *6*, 7408.

(17) Campbell, M. G.; Sheberla, D.; Liu, S. F.; Swager, T. M.; Dincă, M. Cu$_3$(hexaiminotriphenylene)$_2$: An Electrically Conductive 2D Metal-Organic Framework for Chemiresistive Sensing. *Angew. Chem., Int. Ed.* **2015**, *54*, 4349−4352.

(18) Campbell, M. G.; Liu, S. F.; Swager, T. M.; Dincă, M. Chemiresistive Sensor Arrays from Conductive 2D Metal-Organic Frameworks. *J. Am. Chem. Soc.* **2015**, *137*, 13780−13783.

(19) Smith, M. K.; Mirica, K. A. Self-Organized Frameworks on Textiles (SOFT): Conductive Fabrics for Simultaneous Sensing, Capture, and Filtration of Gases. *J. Am. Chem. Soc.* **2017**, *139*, 16759−16767.

(20) Meng, Z.; Aykanat, A.; Mirica, K. A. Welding Metal-lophthalocyanines into Bimetallic Molecular Meshes for Ultra-sensitive, Low-Power Chemiresistrive Detection of Gases. *J. Am. Chem. Soc.* **2019**, *141*, 2046−2053.

(21) Wu, A.-Q.; Wang, W.-Q.; Zhan, H.-B.; Cao, L.-A.; Ye, X.-L.; Zheng, J.-J.; Kumar, P. N.; Chiranjeevulu, K.; Deng, W.-H.; Wang, G.-E.; Yao, M.-S.; Xu, G. Layer-by-Layer Assembled Dual-Ligand Conductive MOF Nano-Films with Modulated Chemiresistive Sensitivity and Selectivity. *Nano Res.* **2021**, *14*, 438−443.

(22) Meng, Z.; Stolz, R. M.; Mirica, K. A. Two-Dimensional Chemiresistive Covalent Organic Framework with High Intrinsic Conductivity. *J. Am. Chem. Soc.* **2019**, *141*, 11929−11937.

(23) Stassen, I.; Dou, J.-H.; Hendon, C.; Dincă, M. Chemiresistive Sensing of Ambient CO$_2$ by an Autogenously Hydrated Cu$_3$(hexaiminobenzene)$_2$ Framework. *ACS Cent. Sci.* **2019**, *5*, 1425−1431.

(24) Wu, J.; Chen, J.; Wang, C.; Zhou, Y.; Ba, K.; Xu, H.; Bao, W.; Xu, X.; Carlsson, A.; Lazar, S.; Meingast, A.; Sun, Z.; Deng, H. Metal-Organic Framework for Transparent Electronics. *Adv. Sci.* **2020**, *7*, 1903003.

(25) Koo, W.-T.; Kim, S.-J.; Jang, J.-S.; Kim, D.-H.; Kim, I.-D. Catalytic Metal Nanoparticles Embedded in Conductive Metal-Organic Frameworks for Chemiresistors: Highly Active and Conductive Porous Materials. *Adv. Sci.* **2019**, *6*, 1900250.

(26) Yao, M.-S.; Lv, X.-J.; Fu, Z.-H.; Li, W.-H.; Deng, W.-H.; Wu, G.-D.; Xu, G. Layer-by-Layer Assembled Conductive Metal-Organic Framework Nanofilms for Room-Temperature Chemiresistive Sensing. *Angew. Chem., Int. Ed.* **2017**, *56*, 16510−16514.

(27) Flynn, S. R.; Wass, D. F. Transition metal frustrated Lewis pairs. *ACS Catal.* **2013**, *3*, 2574−2581.

(28) Sibi, M. P.; Cook, G. R. Copper Lewis Acids in Organic Synthesis. In *Lewis Acids in Organic Synthesis*; Wiley-VCH, 2000; pp 543−574.

(29) Timmons, A. J.; Symes, M. D. Converting Between the Oxides of Nitrogen using Metal-Ligand Coordination Complexes. *Chem. Soc. Rev.* **2015**, *44*, 6708.

(30) Wright, A. M.; Sun, C.; Dincă, M. Thermal Cycling of a MOF-Based NO Disproportionation Catalyst. *J. Am. Chem. Soc.* **2021**, *143*, 681−686.

(31) Sun, L.; Campbell, M. G.; Dincă, M. Electrically Conductive Porous Metal-Organic Frameworks. *Angew. Chem., Int. Ed.* **2016**, *55*, 3566−3579.

(32) Rubio-Giménez, V.; Galbiati, M.; Castells-Gil, J.; Almora-Barrios, N.; Navarro-Sánchez, J.; Escorcia-Ariza, G.; Mattera, M.; Arnold, T.; Rawle, J.; Tatay, S.; Coronado, E.; Martí-Gastaldo, C. Bottom-Up Fabrication of Semiconductive Metal-Organic Framework Ultrathin Films. *Adv. Mater.* **2018**, *30*, 1704291.

(33) Lee, C. Y.; Strano, M. S. Understanding the Dynamics of Signal Transduction for Adsorption of Gases and Vapors on Carbon Nanotube Sensors. *Langmuir* **2005**, *21*, 5192−5196.

(34) Yoon, J.-W.; Kim, J.-H.; Kim, C.; Jang, H. W.; Lee, J.-H. MOF-Based Hybrids for Solar Fuel Production. *Adv. Energy Mater.* **2021**, 2003052.

(35) Koenig, J. Q.; Covert, D. S.; Marshall, S. G.; Belle, G. V.; Pierson, W. E. The Effect of Ozone and Nitrogen Dioxide on Pulmonary Function in Healthy and in Asthmatic Adolescents. *Am. Rev. Respir. Dis.* **1987**, *136*, 1152−1157.

(36) Sadanaga, Y.; Yoshino, A.; Kato, S.; Kajii, Y. Measurements of OH Reactivity and Photochemical Ozone Production in the Urban Atmosphere. *Environ. Sci. Technol.* **2005**, *39*, 8847−8852.